www.ksmrm.org JKSMRM 18(2) : 87-106, 2014
pISSN 1226-9751 / eISSN 2288-3800 http://dx.doi.org/10.13104/jksmrm.2014.18.2.87

Review Article

Towards Routine Clinical Use of Radial Stack-of-Stars 3D Gradient-Echo Sequences for Reducing Motion Sensitivity

Kai Tobias Block[1], Hersh Chandarana[1], Sarah Milla[1], Mary Bruno[1], Tom Mulholland[1], Girish Fatterpekar[1], Mari Hagiwara[1], Robert Grimm[2], Christian Geppert[3], Berthold Kiefer[4], Daniel K. Sodickson[1]

[1]Bernard and Irene Schwartz Center for Biomedical Imaging, New York University School of Medicine, New York, USA
[2]Pattern Recognition Lab, University of Erlangen-Nuremberg, Erlangen, Germany
[3]Siemens Medical Solutions Inc, New York, USA
[4]Siemens AG Healthcare MR, Erlangen, Germany

Purpose : To describe how a robust implementation of a radial 3D gradient-echo sequence with stack-of-stars sampling can be achieved, to review the imaging properties of radial acquisitions, and to share the experience from more than 5000 clinical patient scans.

Materials and Methods: A radial stack-of-stars sequence was implemented and installed on 9 clinical MR systems operating at 1.5 and 3 Tesla. Protocols were designed for various applications in which motion artifacts frequently pose a problem with conventional Cartesian techniques. Radial scans were added to routine examinations without selection of specific patient cohorts.

Results: Radial acquisitions show significantly lower sensitivity to motion and allow examinations during free breathing. Elimination of breath-holding reduces failure rates for non-compliant patients and enables imaging at higher resolution. Residual artifacts appear as streaks, which are easy to identify and rarely obscure diagnostic information. The improved robustness comes at the expense of longer scan durations, the requirement for fat suppression, and the nonexistence of a time-to-center value. Care needs to be taken during the configuration of receive coils.

Conclusion: Routine clinical use of radial stack-of-stars sequences is feasible with current MR systems and may serve as substitute for conventional fat-suppressed T1-weighted protocols in applications where motion is likely to degrade the image quality.

Index words : Radial sampling · Abdominal MRI · Pediatric imaging · Head and neck imaging · Motion robustness, vibe

• Received; April 2, 2014 • Revised; May 28, 2014
• Accepted; May 29, 2014

Corresponding author : Kai Tobias Block, Ph.D.
Bernard and Irene Schwartz Center for Biomedical Imaging, Department of Radiology, New York University School of Medicine, 660 First Avenue, New York, NY 10016, USA.
Tel. 1-212-263-3342, Fax. 1-212-263-7541
E-mail : Tobias.Block@nyumc.org

INTRODUCTION

Almost all clinically established MR imaging techniques today use Cartesian acquisitions of k-space in which the Fourier space of the imaged body is sampled along parallel lines. Cartesian sampling was widely accepted as the standard technique after its first description by Ernst's group in 1975 (1) because parallel-line acquisitions can be implemented with low accuracy requirements for the gradient timing and

because the image reconstruction is a straightforward procedure. However, for many years non-Cartesian sampling schemes have been discussed as potentially superior alternatives. The two most prominent examples are spiral trajectories (2) and radial trajectories, which sample k-space along overlapping spokes (3). While non-Cartesian sequences have been used extensively in basic MRI research (4, 5), in particular in the context of compressed sensing (6), these sequences have not been established in clinical practice, and limited experience exists regarding their usefulness and feasibility for daily routine scanning (except for propeller-type sequences (7) using rotating "blades"made up of parallel lines, for which commercial implementations are available). Obstacles for routine use have been that many of the implementations did not provide the reliability required for clinical imaging or that they involved manual user interaction, such as calibration steps or offline image reconstruction on external computer hardware, which made it difficult to perform large patient studies. On the other hand, non-Cartesian schemes promise to ameliorate some of the current limitations seen with conventional Cartesian MRI. In particular, radial trajectories are known to have significantly lower sensitivity to object motion (8), which poses a major advantage for applications such as abdominal and pediatric imaging where patient motion is a frequent problem.

Recently, we developed a radial 3D gradient-echo sequence with stack-of-stars sampling that integrates seamlessly into clinical workflow. The sequence does not require any additional interaction steps and can be used in a similar way to commercial Cartesian sequences, which enables evaluation of its performance and robustness in daily practice. Results from clinical studies with blinded evaluation by trained radiologists at our and other institutions have been published in a series of research articles for various imaging applications (9–14), demonstrating improved robustness compared to conventional sequences for patients unable to suppress motion. Clinical studies for additional imaging applications are ongoing. The purpose of this overview article is to give comprehensive technical information on the stack-of-stars sequence design, describe how a robust implementation of radial k-space sampling can be achieved, and review the imaging properties of radial acquisitions. Moreover, the experience from over 5000 patient scans acquired over the last 2 years is discussed, aiming to provide a practical starting point for groups that plan to use the described stack-of-stars sequence or other radial sequences in their routine practice.

THEORY

Trajectory Design

The sequence has been derived from a conventional 3D gradient-echo (GRE) sequence with single readout per repetition, which can be used either with non-selective or slab-selective radio-frequency (RF) excitation (15). In the SLICE direction, standard Cartesian phase encoding is performed, while in the READ and PHASE plane data are acquired along radial spokes that are rotated around the center, which results in cylindrical k-space coverage composed of stacked discs ("stack-of-stars", Fig. 1a). Technically, this is realized by playing readout gradients in the READ and PHASE direction simultaneously and modulating the amplitudes according to:

$$G_{READ} = \sin(\Phi) \text{ and } G_{PHASE} = \cos(\Phi). \quad [1]$$

The RF excitation as well as the gradient calculation in SLICE direction remains unchanged from a conventional 3D GRE sequence (see Fig. 2).

Different schemes can be used for selecting the temporal order of the k-space acquisition steps, which has notable impact on the achievable motion robustness and the degree of fat suppression. In our implementation, all phase-encoding steps along the SLICE direction ("partitions") are acquired sequentially before lines at different angular positions are acquired. This ensures that periods of Cartesian sampling are kept short, which leads to high data consistency within the spoke stacks and preserves the motion robustness of radial sampling for the 3D stack-of-stars geometry. Depending on the selected fat-suppression method, the Cartesian phase-encoding steps are performed from the center partition to the k-space periphery (centric out), or in linear order from $-k_{max}$ to $+k_{max}$.

For the angular ordering, the sequence uses either

 http://dx.doi.org/10.13104/jksmrm.2014.18.2.87

equidistant angular sampling with multiple interleaves or the golden-angle scheme. In the equidistant scheme (Fig. 1b), the angular distance is calculated according to

$$\Delta\Phi = 180^\circ / n_{total}$$

where n_{total} is the total number of spokes. It turned out to be beneficial to acquire the spokes using multiple interleaves (or "rotations") because the interleaving reduces temporal coherences in k-space. Thus, motion inconsistencies are spread out in k-space and artifacts are visually attenuated. Usually, we use $n_{rot} = 8$ interleaves where spokes have an angular distance of $n_{rot} = 180^\circ\ n_{rot} / n_{total}$ and subsequent interleaves are rotated by $\Delta\Phi$. Furthermore, the orientation of every second spoke is alternated, i.e. addition of 180°, so that adjacent spokes in k-space have opposing orientation, which reduces the sensitivity to motion and the visual impact of off-resonance effects.

In the golden-angle scheme (Fig. 1c), the angle is increased each time by $\Delta\Phi GA = 111.25^\circ$, which corresponds to 180° multiplied by the golden ratio (16). Therefore, subsequently sampled spokes always add complementary information while filling the largest gaps within the previously sampled spokes. As consequence, any sequential set of acquired spokes covers k-space approximately uniformly, which enables reconstruction of temporal subframes and makes the golden-angle scheme very interesting for dynamic imaging studies (16). Additional interleaving or alternation of spokes is not needed for this scheme.

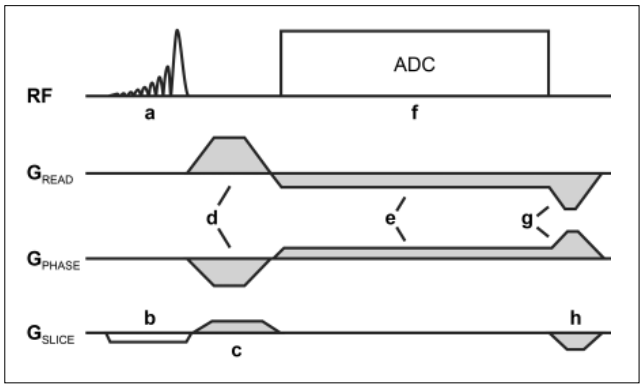

Fig. 2. Basic pulse sequence diagram for one TR repetition cycle, starting with a RF excitation pulse (**a**), which is used either without or with slab-selection gradient (**b**). Gradient pulse (**c**) combines slab-selection rewinding and Cartesian phase encoding along the SLICE axis. Gradient pulses (**d**) act as dephasing, (**e**) readout, and (**g**) spoiling gradients in the READ-PHASE plane. Gradients (**d**, **e**, **g**) are played simultaneously in the READ and PHASE direction with amplitudes modulated according to Eq. (1), resulting in radial k-space traversal. The signal is recorded using an ADC event (**f**) during the flat-top time of the readout gradients (**e**). Gradient pulse (**h**) spoils residual magnetization along the SLICE axis. Gray color indicates that gradient amplitudes are changing per repetition.

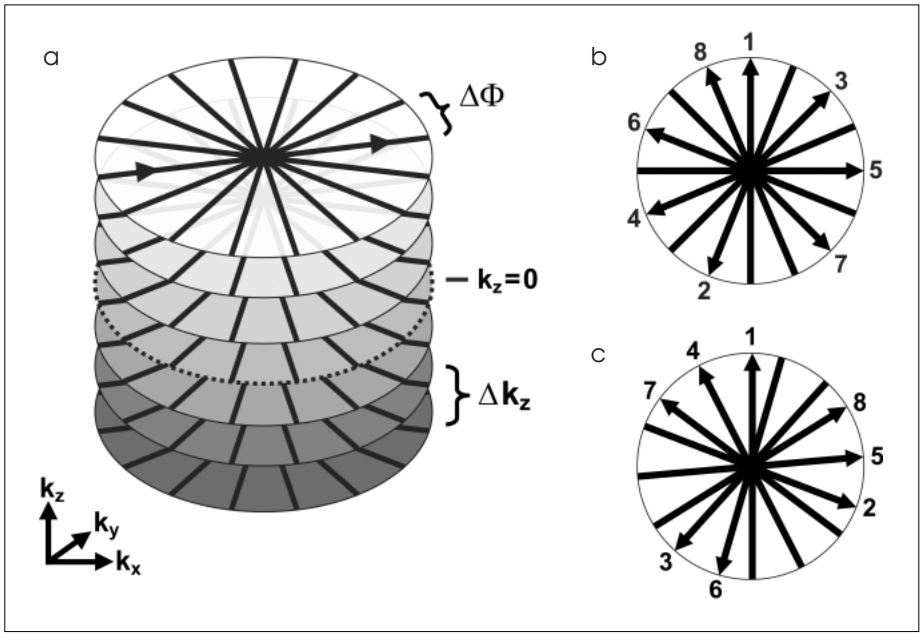

Fig. 1. (**a**) "Stack-of-stars" trajectory, which acquires the kx-ky plane along radial spokes and the kz direction with Cartesian sampling. The angle of the radial spokes can be ordered (**b**) using an equidistant scheme or (**c**) using the golden-angle scheme. Numbers indicate the temporal order of the acquisition.

Image Reconstruction

Because the sample locations along rotated spokes do not fall on an equidistant grid, which is required for applying the fast Fourier transform (FFT) algorithm, it is not possible to use conventional FFT-based image reconstruction for radially sampled data. Thus, it is necessary to interpolate the data onto a regular grid at some point during the reconstruction. Classically, two different approaches have been used for image reconstruction from radial data: filtered back projection (FBP) and convolution-based gridding, which is also known as regridding or non-uniform FFT (NUFFT). Both approaches are basically equivalent and differ only in the interpolation step (17): in FBP the interpolation is performed in image space, whereas in gridding it is done in k-space. Because the gridding approach offers higher flexibility for data correction in k-space, it has been preferred and implemented for the sequence.

The gridding procedure essentially comprises 1) weighting of the data with a density compensation function (DCF) to compensate for the overlap of samples in the k-space center, which for the radial geometry is the RamLak or M-filter

DCF = |k| (18), 2) convolution of all samples with an interpolation kernel and evaluation on a regular grid, 3) FFT of the gridded data, and 4) multiplication with a roll-off correction function to compensate for the k-space convolution with an imperfect interpolation kernel. A detailed description of the gridding method is given in (19). Here, a Kaiser-Bessel interpolation window of size 3 has been used with shape parameter a = 4.2054 according to the nomenclature used in (19). The intensity modulation for the roll-off correction is obtained by placing the interpolation window in the center of an empty matrix and calculating the FFT. As discussed in the literature (19, 20), the interpolation error can be reduced by interpolating the data on a twofold-oversampled matrix and cropping the FOV after the FFT. Because the sequence acquires data already with twofold readout oversampling, the received samples can be gridded on a matrix of matching dimension.

Prior to running the gridding procedure, a FFT is applied to all radial sample locations along the SLICE dimension to remove the Fourier encoding in this direction. Afterwards, the gridding procedure can be applied to all slices separately, which enables processing slices in parallel to achieve clinically feasible reconstruction times. This poses an advantage over ball-shaped radial 3D trajectories, which require gridding in 3D and are more difficult to parallelize. To handle data from receive-coil arrays, separate images are reconstructed for each receive channel and combined using the sum-of-squares approach.

Sampling Properties

Changing the sampling pattern from parallel lines to

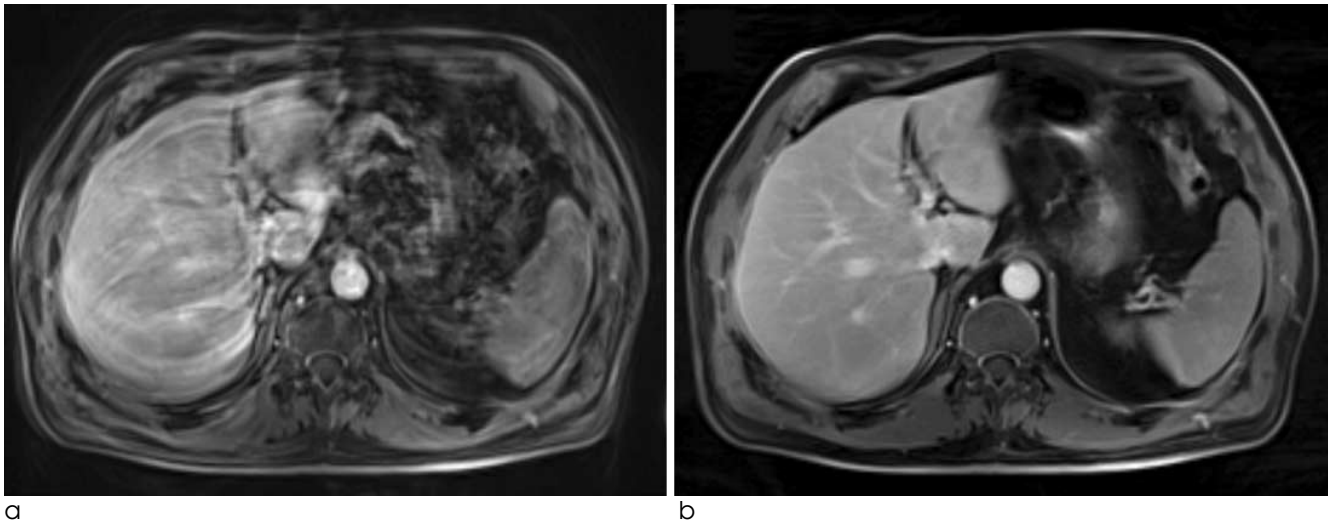

a b

Fig. 3. Free-breathing abdominal exam using (**a**) conventional Cartesian sampling and (**b**) radial sampling (with otherwise identical sequence parameters and matching acquisition time). While the Cartesian scan suffers from strong "ghosting"artifacts, the radial acquisition provides diagnostic image quality.

http://dx.doi.org/10.13104/jksmrm.2014.18.2.87

overlapping spokes introduces unique imaging properties, which are in part advantageous and in part disadvantageous for clinical applications. One key advantage is the significantly higher robustness to object motion compared to the rather sensitive Cartesian scheme (Fig. 3), which can be explained by two effects. First, the overlap of spokes in the k-space center creates a time-averaging effect, so that motion averages out over the acquisition window, in particular for longer scan durations. Second, due to the varying readout directions, object movements do not translate into shifted image copies ("ghosting") as for Cartesian sampling. In Cartesian scans, adjacent phase-encoded k-space lines need to have a constant phase difference. Because translations in image space lead to phase offsets in k-space, which distort the phase encoding and can be interpreted as jittering the motion-affected lines in k-space, the Nyquist theorem is violated due to the motion. Thus, image copies appear from aliasing that contaminate the FOV along the phase-encoding direction, which often render the images non-diagnostic (Fig. 3a).

This is completely avoided when rotating the sampling direction in k-space. In this case, object motion can lead to local image blurring and to streak artifacts that radiate from the motion affected regions. However, usually the streaks are minor and it is possible to read through the artifacts, in particular because radiologists are trained to read images with streak artifacts, which also appear in computed tomography (CT) studies. In fact, it is a significant advantage of radial sampling that artifacts are easy to identify due to their distinct visual appearance and that they tend to merely add texture-like patterns rather than obscuring structures (see Fig. 9d for an example).

Another advantage of rotating the readout direction is that readout oversampling can be applied along both the READ and PHASE directions without increasing the scan duration. Therefore, it is possible to reduce the FOV size below the object extent without appearance of aliasing (Fig. 4), which increases protocol flexibility and reduces the need for patient-specific FOV adjustments. In contrast, for Cartesian trajectories oversampling in the PHASE direction increases scan time linearly and, thus, its applicability in routine scans is limited.

As a disadvantage, radial trajectories have higher sampling requirements due to the less efficient coverage of k-space, which can pose a limitation for time-critical acquisitions like breath-hold scans. A common rule for selecting the number of spokes is $\pi/2$ * base resolution (matrix size), which ensures that the largest angular distance is $\Delta k = 1/FOV$ to comply with the Nyquist criterion for Cartesian sampling. However, this should be seen more as a rule of thumb rather than a strict criterion. Figure 5 shows the point spread function (PSF) for a radial trajectory, which has a central peak surrounded by a dense disc with almost uniform intensity (despite minor oscillations from Gibbs ringing). The radius of the disc is often called Nyquist radius and depends on the number of acquired spokes. Beyond this radius, the PSF shows radially propagating streaks.

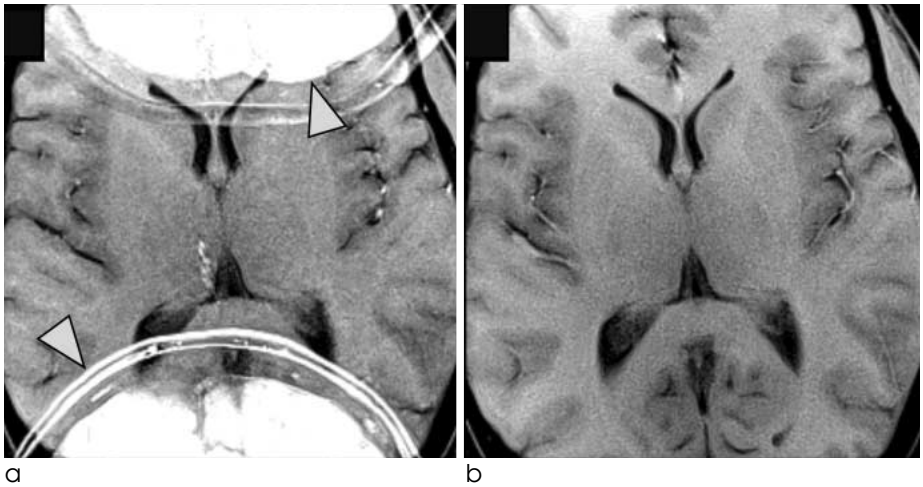

Fig. 4. Scan with reduced FOV size using (**a**) Cartesian sampling and (**b**) radial sampling. Due to the large object extent, aliasing occurs with Cartesian sampling along the phase-encoding direction. Because readout oversampling can be applied in both directions, aliasing does not appear with radial sampling.

According to the PSF description of the imaging process, the object is convolved with the PSF as consequence of the discrete signal acquisition in k-space and, thus, depicted without streak artifacts when the largest object diameter is equal to or smaller than the Nyquist radius. Hence, if the object extent coincides with the selected FOV size, the rule mentioned above correctly determines the number of needed spokes. However, often the object is larger than the selected FOV (e.g., if the arms are placed next to the body for abdominal studies) and in this case streaks can appear from the convolution of the outer-FOV intensities with the PSF (note that areas outside the FOV contribute to the received signal even if these areas are cropped and not visible in the final image). Thus, more spokes may be needed to completely avoid streaks in the reconstructed image. On the other hand, if the object does not completely fill the FOV, fewer spokes are sufficient to obtain an image without visible streaks. Hence, the number of actually required spokes depends on the object diameter and not solely on the selected base resolution.

For some applications, a certain degree of streaking may be tolerable when high imaging speed is required. In this case, the number of spokes can be reduced to lower the number of sequence repetitions. Higher reduction factors lead to more pronounced streak artifacts (Fig. 5), while the underlying spatial resolution remains unchanged, as it is defined by the full width at half maximum (FWHM) of the central PSF peak (21). The flexibility to undersample data by a continuous factor is another advantage over Cartesian sampling and can be helpful when modifying protocols to match timing constraints. Notably, for moderate undersampling levels images are usually still of diagnostic value even without use of a parallel-imaging technique.

When imaging speed is not the highest priority, it can be advantageous to acquire more spokes than strictly required because this reduces motion artifacts and improves the signal-to-noise ratio (SNR). In this

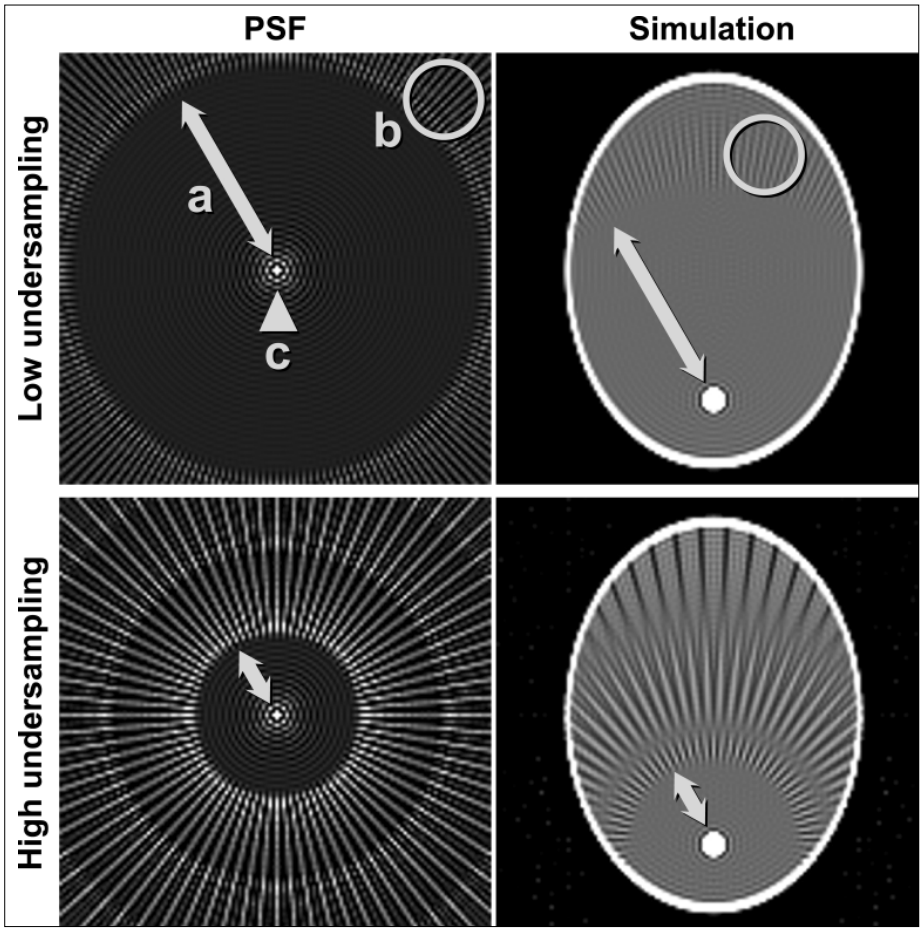

Fig. 5. (Left) Radial point-spread-function and (right) exemplary imaging simulation for (top) mild and (bottom) strong undersampling. The PSF has a central peak (**c**), which reflects the obtained spatial resolution and whose width is independent of the undersampling. It is surrounded by a dense disc with minor circular Gibbs ringing. Beyond the Nyquist radius (**a**), which depends on the number of acquired spokes, it shows radially propagating streak patterns (**b**). The high-intensity circle of the simulation object therefore leads to streaks in the reconstructed image at Nyquist distance. A streak-free image is obtained if the largest object diameter is smaller than the Nyquist radius.

http://dx.doi.org/10.13104/jksmrm.2014.18.2.87

case, the intensities seen in the image reflect the probability of localization during the acquisition period. Static areas appear bright and sharp whereas motion-affected areas are smudged out along their motion trajectory. Such effects are often seen, for instance, at the tip of the liver in abdominal scans. Hence, unlike Cartesian sequences where scan durations are usually minimized to avoid motion inconsistencies and associated ghosting artifacts, radial protocols can be designed with long acquisition times, enabling high spatial resolution and good reproducibility across patients.

However, because all of the spokes pass through the center of k-space and contribute equally to the reconstructed image, the obtained image contrast represents an average over the entire scan duration, and a time-to-center value does not exist. While this property results in higher scan consistency and reduced sensitivity to timing inaccuracies for post-contrast exams, it also means that the vessel-tissue contrast is usually lower than for Cartesian sequences where the bolus arrival can be timed to coincide with the acquisition of the k-space center (9, 10). Because sampling of k-space center information starts right in the beginning of acquisition, radial scans also require a higher number of preparation shots to avoid artifacts from the transition to steady state, whereas in Cartesian schemes the initial acquisitions can be used for sampling outer k-space lines that are less susceptible to steady-state effects. In our applications, the number of preparation excitations is typically set to 60 times the number of partition steps along the SLICE direction.

Gradient-Delay Compensation

A significant problem for practical use of radial sampling consists in the required high timing accuracy of the created gradient fields. Gradient fields often show delayed response as well as overshooting (22, 23), which for sequences with straight readouts results in k-space shifts along the readout direction. For Cartesian sequences, this effect is negligible because all lines experience an equal unidirectional shift, causing just a linear image phase that is not visible in magnitude reconstructions. However, for radial sequences, the readout orientation varies per repetition and, thus, the trajectory gets distorted due to the shifts along different directions. This results in streak-alike artifacts at the border of the object as well as in intensity modulations and image blurring (Fig. 6a). In the recent generation of MR systems, the strength of the gradient-delay effects has been reduced significantly compared to older systems, but especially at high readout bandwidths artifacts remain visible. Alternating the orientation of even and odd spokes (as described in Trajectory Design) helps to attenuate the artifacts to some degree. However, in order to provide reliable image quality across the whole range of bandwidth settings, we implemented an adaptive compensation of gradient delays.

For radial trajectories, the gradient delays primarily cause a signal shift along the readout direction while off-center displacements, as obtained for severe gradient anisotropies (23), were of minor significance

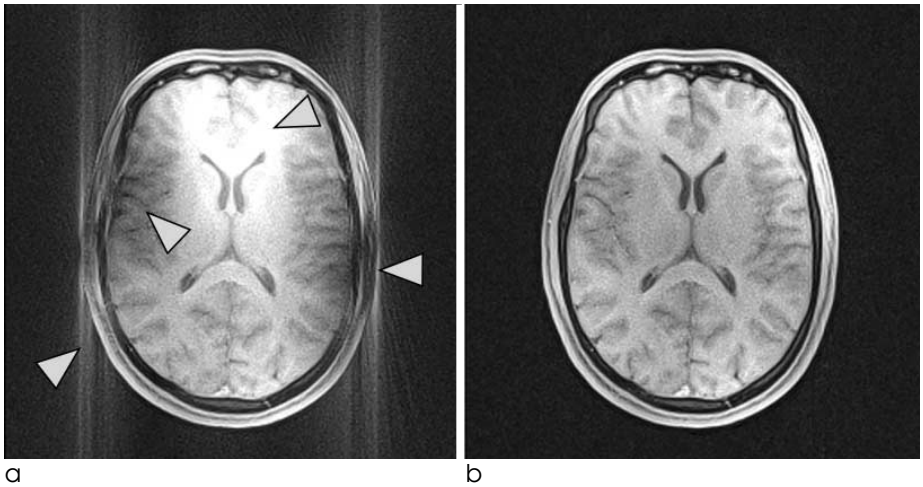

Fig. 6. (**a**) Without correction of gradient delays, radial scans suffer from intensity modulations and streaks around the object. (**b**) Corrected radial scan after applying the described adaptive calibration approach.

on the systems used in this work. Therefore, the shift in k-space can be estimated by acquiring a set of calibration spokes with opposing orientation (0° and 180° for G_x, 90° and 270° for G_y). By performing a cross-correlation analysis of the signals, the echo distance between the forward and backward acquisition can be estimated in sample units, which corresponds to twice the echo shift that every spoke experiences. Details of the algorithm have been described in (24). Because performing preparation shots is mandatory for radial GRE sequences as discussed above, these preparation excitations can be employed to acquire the calibration data. In this way, the gradient-delay estimation does not prolong the overall scan time and multiple averages of calibration data can be acquired to improve the accuracy. Noteworthy, because the echo-pixel shift is estimated from the sampled calibration signals regardless of the actual origin of the shift, the method inherently also accounts for delays caused by timing inaccuracies of the signal-receive hardware and possibly eddy-current effects. Correction of the delays is finally possible by adjusting the k-space locations of the samples in the gridding procedure according to the estimated echo-pixel shifts (Fig. 6b). An additional correction for eddy-current-induced phase perturbations was not necessary on the MR systems used here.

Off-Resonance Sensitivity and Fat Suppression

Off-resonant signal components like fat cause the well-known chemical-shift artifact for Cartesian acquisitions because the deviating resonance frequency leads to a linear phase evolution along the readout direction, which translates into a unidirectional spatial shift in image space (with the shift distance depending on the acquisition bandwidth, Fig. 7a). When using radial sampling, the off-resonant signal components are shifted in a different spatial direction for each acquired spoke, which results in signal blurring instead of a unidirectional shift (Fig. 7b). The strength of the blurring depends again on the readout bandwidth (with higher bandwidth resulting in reduced artifacts). Usually, the blurring has more severe impact on the overall image quality than conventional chemical-shift artifacts. Especially in applications that require low bandwidth settings to gain SNR, off-resonant signal components can render radial acquisitions completely non-diagnostic. Alternating the orientation of even and odd spokes helps to attenuate the visual impact of the blurring, but the artifacts remain problematic.

Therefore, the sequence should generally be used

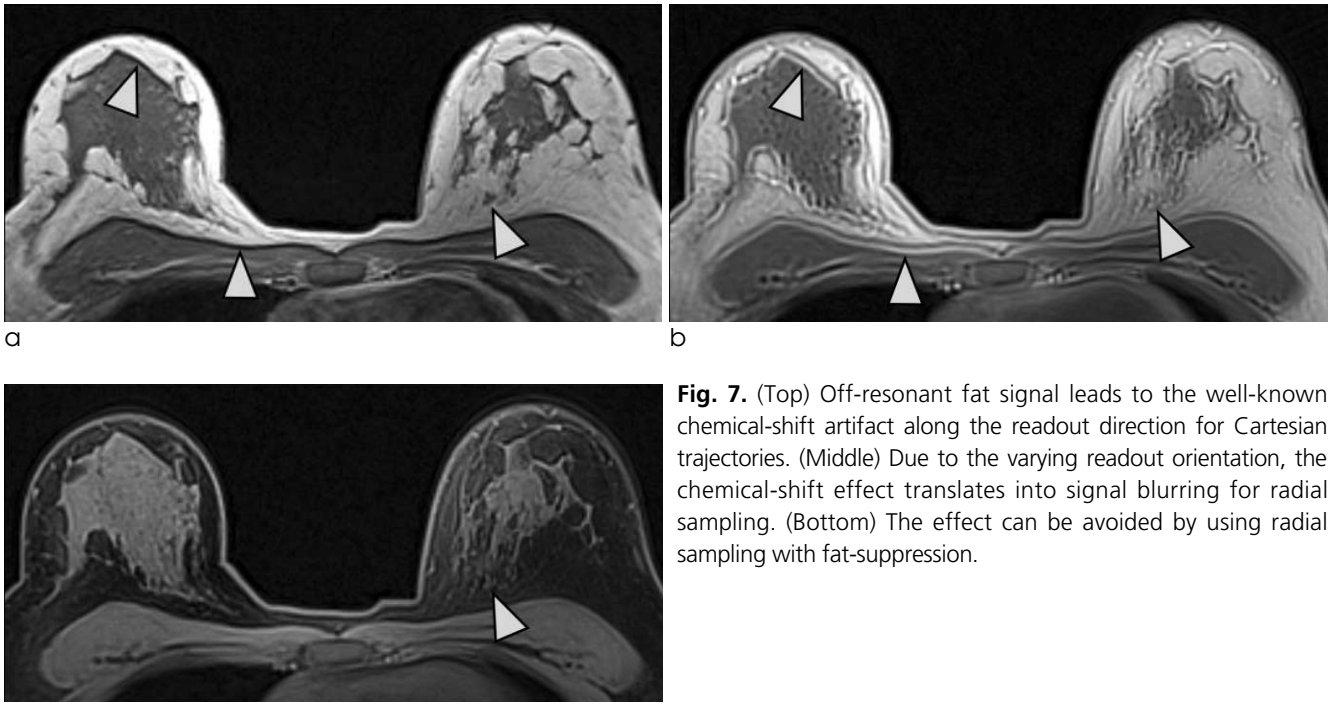

Fig. 7. (Top) Off-resonant fat signal leads to the well-known chemical-shift artifact along the readout direction for Cartesian trajectories. (Middle) Due to the varying readout orientation, the chemical-shift effect translates into signal blurring for radial sampling. (Bottom) The effect can be avoided by using radial sampling with fat-suppression.

http://dx.doi.org/10.13104/jksmrm.2014.18.2.87

with fat suppression (Fig. 7c), unless very high readout bandwidth is used. Different fat-suppression techniques have been implemented, including water excitation (WEX), spectral fat saturation with multiple readouts (Quick FatSat), and spectral adiabatic saturation with multiple readouts (SPAIR). Performing multiple readouts after a single saturation pulse is possible for the stack-of-stars geometry when using the described ordering scheme, which acquires all partitions sequentially for each angle. If a single saturation pulse is created for each angle, all partitions experience a consistent degree of fat suppression, which avoids in-plane artifacts from spokes with varying fat contribution and allows adjusting the saturation pulse to yield optimal fat suppression during acquisition of the center partition.

WEX and SPAIR give better fat-suppression quality at the price of higher scan time and may be used for applications that require precise anatomical definition such as breast imaging. For most other applications, Quick FatSat provides sufficient fat-saturation quality and is favorable due to the higher acquisition speed. DIXON-based multi echo fat/water separation is theoretically also possible for radial acquisitions but conventional approaches cannot be applied in a straightforward manner because they do not remove the blurring of the fat signal (25). A technique tailored for use with the sequence is currently under development.

Coil Considerations

Radial sequences can be used with any birdcage coil or array of surface-coil elements. However, inappropriate placement of receive-coil elements (or, inclusion of improperly located coils into the reconstruction) can lead to severe streak artifacts, which turned out to be the leading source of image-quality issues in our evaluation phase. As discussed in the Sampling Properties section, the intensities received by each coil are convolved with the PSF of the sampling trajectory, resulting in streaks beyond Nyquist distance from the source intensities. Thus, if coil elements are included that have their main sensitivity localization far away from the region of interest (ROI), these coils will predominantly contribute streaks to the ROI of the combined image. Figure 8a shows a coronal thorax scan with severe streak artifacts in the lung. These artifacts originate from a coil positioned in the pelvic area below the FOV. When disabling this coil, as done in Figure 8b, the artifacts disappear and a high-quality image is obtained without noticeable signal loss in the ROI.

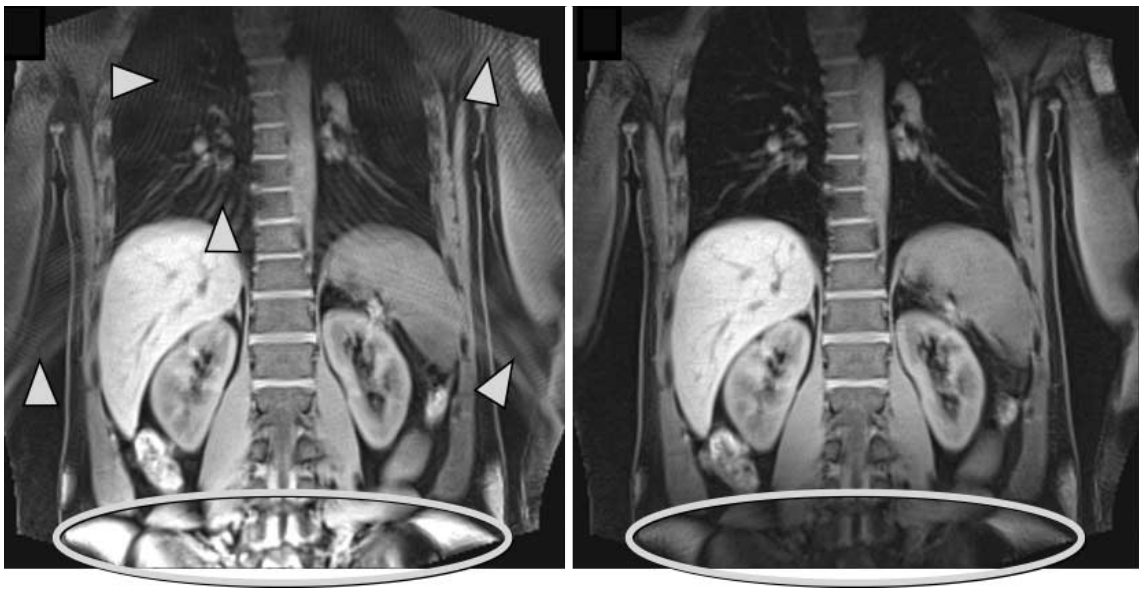

Fig. 8. (**a**) Severe streak artifacts appear in the thorax (arrows), which are caused by an improperly selected coil element with main sensitivity localization in the pelvic area (circle). (**b**) After disabling the coil, the streak artifacts disappear with negligible loss of the overall signal intensity in the region-of-interest.

Hence, it is important to disable coil elements at distant locations from the ROI, particularly because gradient nonlinearities may cause signal concentration away from the isocenter, which tends to spill severe streak artifacts into the ROI (26). Furthermore, spectral fat-suppression techniques often fail at the periphery due to B0 inhomogeneities, which can lead to streak artifacts in the ROI when the high-intensity fat signal is taken up by distant coils. We therefore instruct our technicians to manually select only those coil elements that directly cover the ROI and to verify the coil setup before every scan, which resolved most of the image-quality issues initially seen. In future versions of the scanner software, this problem may be prevented by introducing a more restrictive automatic coil-selection mechanism for radial scans.

When a choice between different coil designs exists, it is usually preferable to select coil arrays with rather broad sensitivity of the individual elements. High-density coils with localized sensitivity (focused on the object surface) tend to cause stronger streak artifacts, which radiate from the high-intensity spots of the elements. This can be seen, e.g., in free-breathing abdominal scans because high receive sensitivity is placed on the moving abdominal wall. Furthermore, the stronger intensity gradient towards the center of the object makes it necessary to use image-intensity normalization. Normalizing the image intensity is often accompanied by visual amplification of streak and noise patterns in the low-intensity areas.

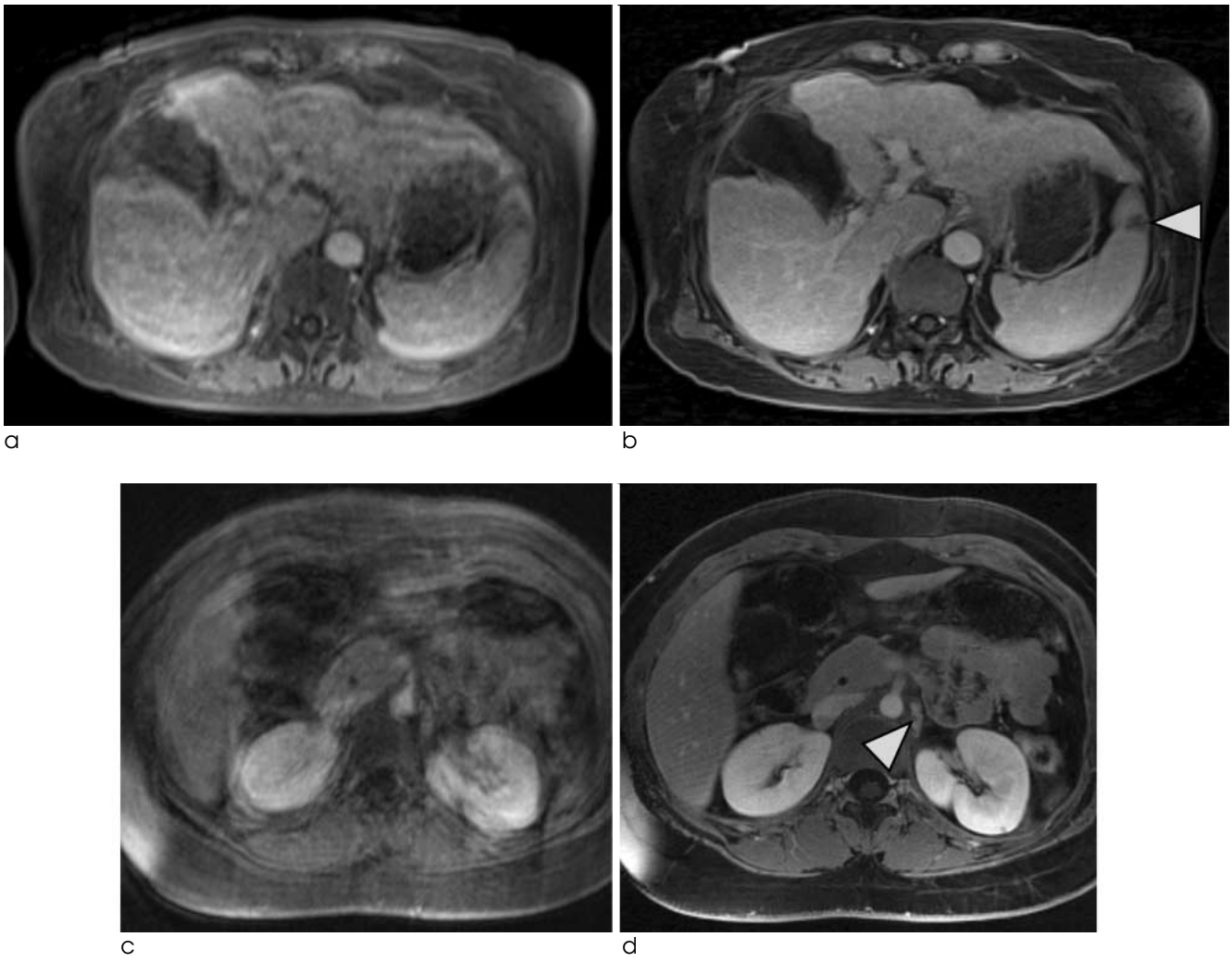

Fig. 9. (**a, c**) Cartesian 3D GRE exam of the liver in patients unable to suspend respiration, compared to (**b, d**) examination during free breathing using the radial sequence. A lesion in the spleen (arrow in **b**) is only visible on the radial exam. An enlarged lymph node (arrow in **d**) is clearly identified on the radial exam but difficult to appreciate on the Cartesian exam.

http://dx.doi.org/10.13104/jksmrm.2014.18.2.87

Therefore, we usually try to avoid image normalization, which is less problematic with low-density coils.

Implementation and Clinical Evaluation

The sequence has been implemented using the IDEA development environment (Siemens AG, Healthcare Sector, Erlangen, Germany) and has been installed on 9 different clinical MR systems with field strengths 1.5 Tesla and 3 Tesla, including MAGNETOM Avanto, MAGNETOM Verio, MAGNETOM Trio, and Biograph mMR (all from Siemens AG, Healthcare Sector, Erlangen, Germany). The sequence code was derived from the VIBE product sequence (version VB17A) and modified as described in the Theory section. The gridding-based image reconstruction was implemented in the ICE framework using pre-calculation of interpolation coefficients, which are shared across slices. With parallelized reconstruction of 4 slices at the same time, the achieved reconstruction speed on standard hardware was fast enough for routine use without compromising clinical workflow.

Scan protocols were added to routine examinations for various clinical indications without selection of a specific patient cohort. The total added exam time was restricted to 7 minutes, complying with the guidelines of our institutional review board (IRB) for technical developments. It was ensured that no interference with clinically required imaging occurred. Images were sent to the PACS server along with routine scans but were not used for primary reading. At the time of

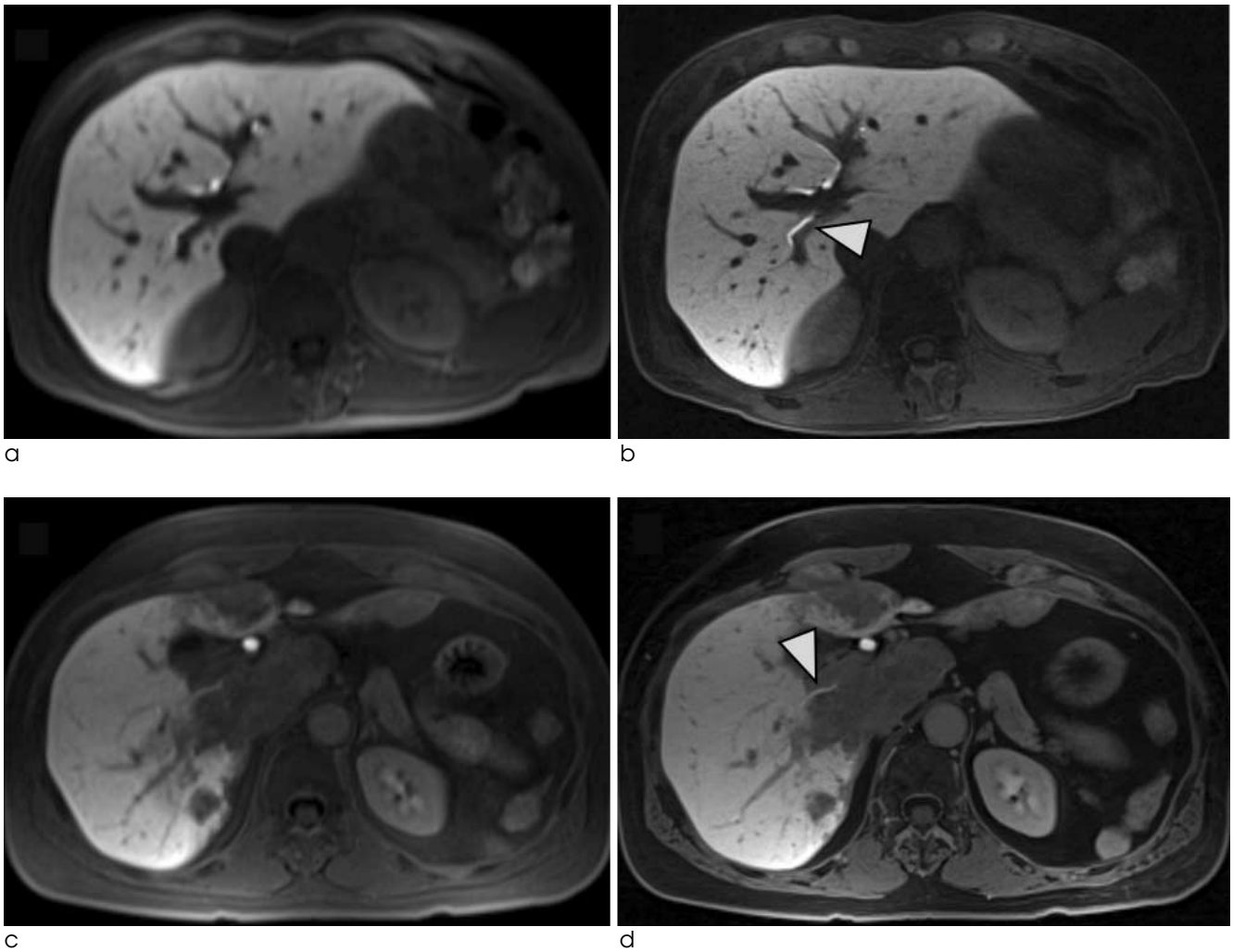

Fig. 10. (**a, c**) The achievable resolution with Cartesian scans is limited by the typical breath-hold capacity of less than 20 sec. (**b, d**) Radial acquisition during free shallow breathing enables to obtain significantly higher spatial resolution. In the example of late-phase exam after injection of EOVIST, it provides much sharper depiction of the biliary duct (arrows).

writing, our PACS contained 5253 clinical datasets acquired using the described sequence.

Protocol parameters were selected to match the imaging requirements of the individual clinical application and are discussed in the following section for representative examples. Of note, quantitative assessments of the image quality in these applications have been presented in the related references and are not repeated here. As a general guideline, the sequence should be used with base resolutions from 224 – 384 pixels and 400 – 800 spokes. Reasonable values for the number of slices range between 48 – 196, where reduced slice resolution, i.e. acquisition of fewer partitions with zero-padded reconstruction, of up to 60% and partial Fourier factors of up to 6/8 can be used to shorten scan time. For 3 Tesla scans, bandwidths of 300 – 800 Hz/pixel are reasonable values, while for 1.5 Tesla systems 200 – 600 Hz/pixel should be used. Usually, a smaller FOV size than in Cartesian protocols is chosen, which can help to reduce the base resolution and angular sampling requirements. For most applications, timing settings

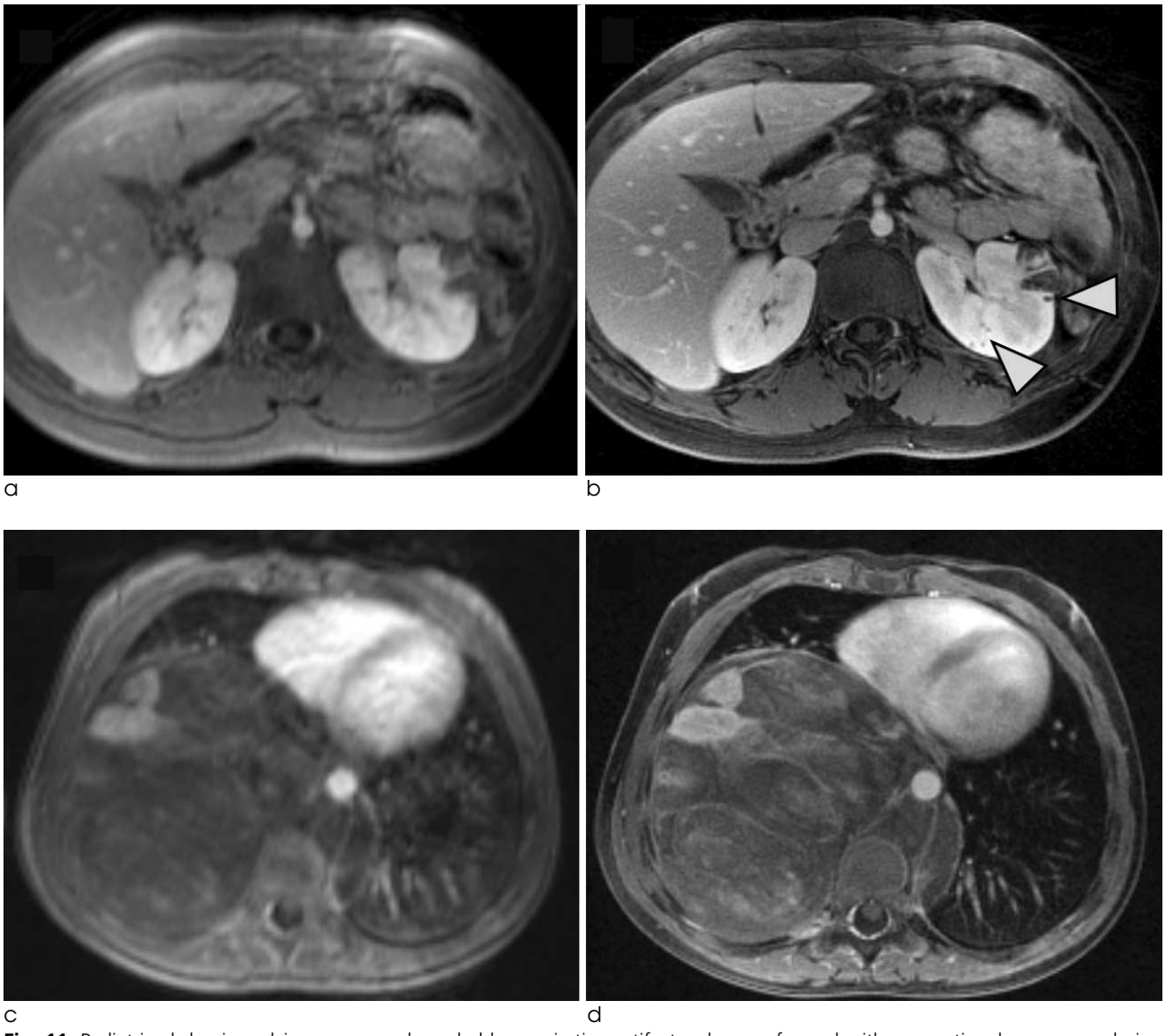

Fig. 11. Pediatric abdominopelvic exams are degraded by respiration artifacts when performed with conventional sequences during sedation (**a, c**), which limit the effective resolution. Significantly improved image quality is achieved with the radial sequence (**b, d**). In the case of a patient with Tuberous Sclerosis (top), the radial sequence reveals small cysts in the kidney (arrows).

http://dx.doi.org/10.13104/jksmrm.2014.18.2.87

with minimal possible echo time (TE) and repetition time (TR) are preferable to achieve high scan efficiency. When high fat-saturation quality is needed on 3 Tesla systems, it can be beneficial to run the sequence with TE meeting the opposed-phase condition rather than with minimal TE. Reasonable flip-angle values for T1-weighted contrast range between 9° and 12°.

CLINICAL APPLICATIONS

Example 1: Free-Breathing Abdominal MRI

Due to the high motion sensitivity, conventional T1-weighted abdominal exams generally have to be acquired during breath holding. With typical scan durations of 15 – 20 sec, many patients struggle to suspend respiration during the exam and severe motion artifacts are seen frequently, especially for elderly, severely sick, and incompliant patients. Figure 9 demonstrates in two patient cases that diagnostic images with comparable quality to normal breath-hold scans can be obtained during free shallow breathing using the radial sequence (Fig. 9b/d), which therefore can be the preferable strategy for pre- and post-contrast exams in patients incapable to hold breath. For this application, 64 – 88 slices with 400 spokes and a base resolution of 256 pixels were acquired using a bandwidth of 400 Hz/pixel at 1.5 Tesla and 600 Hz/pixel at 3 Tesla, resulting in scan times between 60 sec and 90 sec. Evaluations of the image quality in comparison to conventional breath-hold exams have been presented in (9, 10, 14).

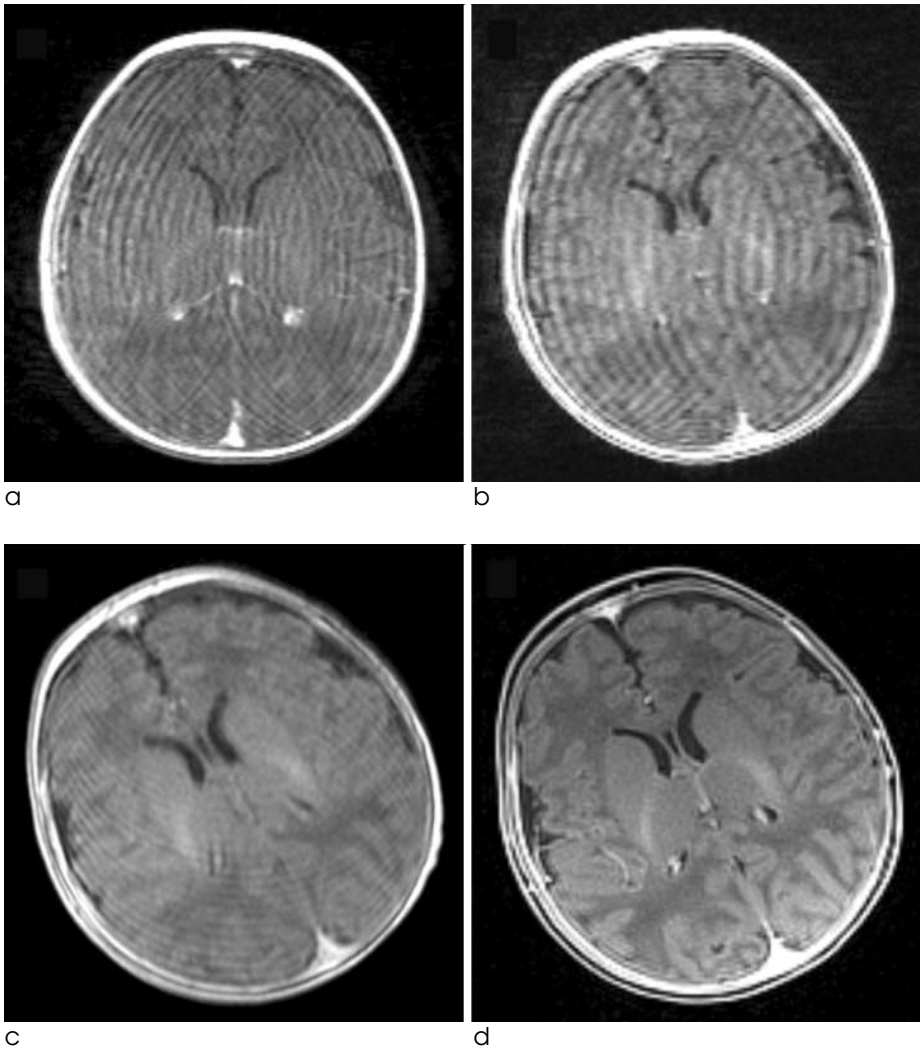

Fig. 12. Brain exam of a 4-week-old active patient using (**a**) 2D TSE, (**b**) MP-RAGE, (**c**) 2D FLASH, and (**d**) the radial sequence. While all Cartesian sequences were affected by a certain level of motion artifacts, the radial sequence provided acceptable diagnostic image quality.

Example 2: High-Resolution Liver Imaging

The requirement to perform exams during suspended respiration inherently limits the spatial resolution achievable with Cartesian acquisitions, even for patients with proper breath-holding capability. Because radial acquisitions can be performed during continued shallow respiration, it is possible to acquire data for several minutes, which enables obtaining images with significantly higher resolution than for breath-hold exams. Figure 10 shows the resolution improvement for late-phase acquisitions after injection of gadoxetate disodium (EOVIST, Bayer HealthCare Pharmaceuticals, Wayne, NJ), which yield sharp visualization of the vessel anatomy and biliary duct. These exams are possible during free breathing because the contrast-enhanced liver tissue has high signal strength relative to surrounding tissues (especially when using flip angles up to 25°), which reduces the sensitivity to streaks from bowel or abdominal-wall motion. In this application, the base resolution was increased to 384 pixels and the number of spokes to 900, resulting in 1.0 mm resolution. Depending on the required spatial coverage and slice thickness between 1.0 – 2.0 mm, the scan time ranges typically between 4 to 6 min.

Example 3: Pediatric Body Imaging

Pediatric body scans are particularly challenging exams because patient cooperation is usually low. Younger patients often have to be examined during deep sedation or general anesthesia, which precludes active breath holding during the scans. Therefore, images acquired with Cartesian sequences are always affected by a certain degree of respiration artifacts, which limit the sensitivity for smaller pathologies. Radial sampling offers significant improvement of

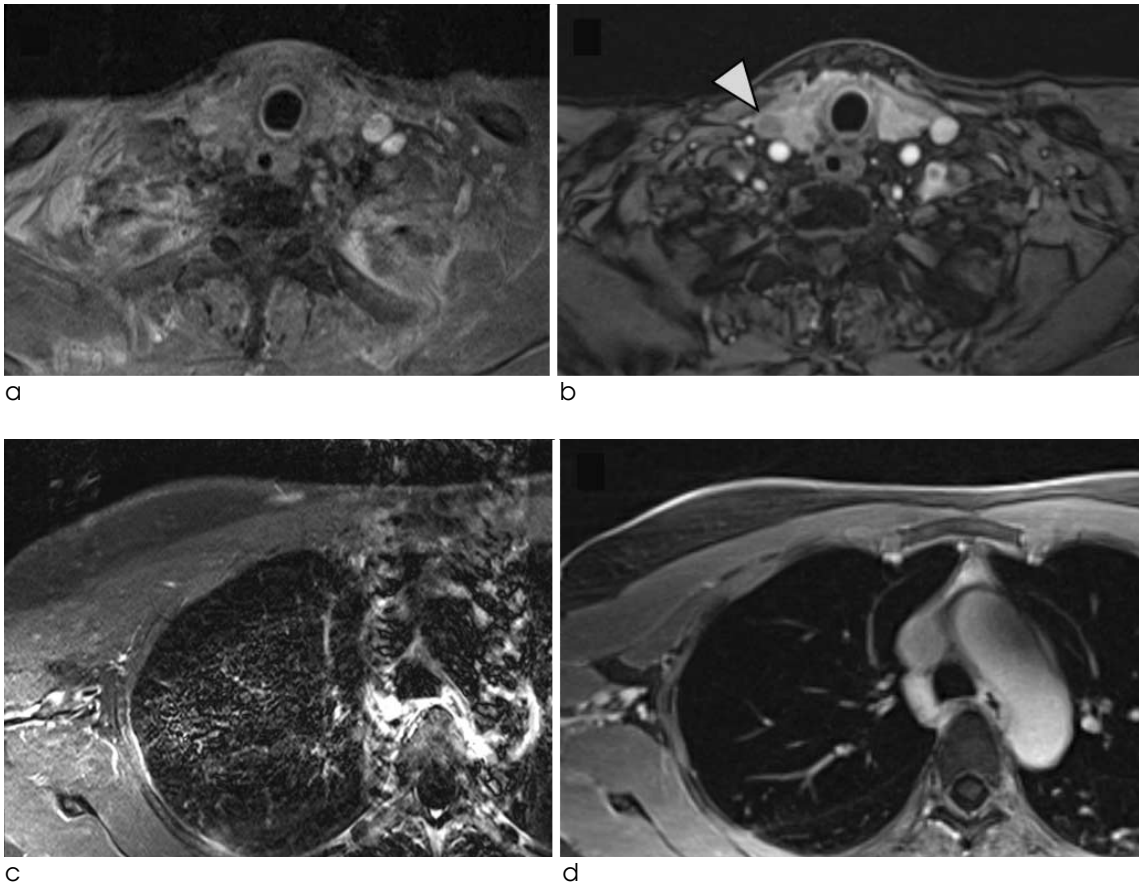

Fig. 13. Imaging of the neck (**a, b**) and upper chest (**c, d**) using a conventional 2D TSE sequence (**a, c**) and the radial sequence (**b, d**). Due to strong motion and flow artifacts, a mass in the thyroid gland is not visible on the 2D TSE exam but appreciated on the radial scan (arrow in **b**). Evaluation of the sternum in a patient complaining of pain was not possible on the 2D TSE scan (**c**), but unproblematic with the radial sequence (**d**).

http://dx.doi.org/10.13104/jksmrm.2014.18.2.87

these exams, providing much sharper and more consistent images. Figure 11 demonstrates the achievable image-quality gain for breathing sedated patients. Of note is the much sharper depiction of small cysts in the kidneys of a patient with Tuberous Sclerosis. For these scans, a high number of 800 spokes with base resolution of 256 pixels was acquired over 3 – 4 min to minimize motion blurring. An assessment of the image quality has been presented in (11) and demonstrated that in an average of 15% of the cases, lesions were only seen with radial acquisition.

Example 4: Pediatric Brain Imaging

The sequence also demonstrated high value for imaging of the pediatric brain. In young neonatal patients where physical immobilization is preferred over sedation, residual motion often degrades the image quality, especially when patients show increased activity after contrast injection. Figure 12 compares different T1-weighted sequences that were repeatedly acquired due to vigorous head motion of a 4-week-old patient. While all Cartesian sequences were affected by a certain amount of motion artifacts, clean image quality was obtained with the radial sequence. Here, 800 spokes were acquired in a scan time of 7 min for full head and neck coverage with 160 slices (0.94 mm isotropic resolution, 280 Hz/pixel at 1.5 Tesla).

Example 5: Imaging of the Neck and Upper Chest

Imaging of the neck is often impeded by artifacts when patients are unable to suppress swallowing or coughing, especially if lesions compress the trachea. Conventionally, these scans are performed with turbo spin-echo (TSE) sequences, which are very susceptible to motion and pulsation artifacts. Strong artifacts also arise in the upper chest region because the required high spatial resolution precludes that the acquisition can be performed during breath holding. Figure 13 demonstrates that the radial sequence provides significantly cleaner images in these regions and is capable of providing diagnostic information in cases where conventional protocols are difficult to read. The improvement in image quality was evaluated in a blinded fashion in (12) and discussed for lung-nodule detection in (13). We currently perform these scans in axial orientation with 1.0 mm isotropic resolution as shown in Figure 14, which are in most cases free from any motion artifacts and show only minor blurring even for rather vigorous patient activity (240 slices with 1 mm isotropic resolution, 610 Hz/pixel at 3 Tesla, 7 min scan time). Furthermore, multi-planar reconstructions (MPR) can be generated from these scans, eliminating the need of acquiring redundant 2D sequences in multiple orientations as routinely done in

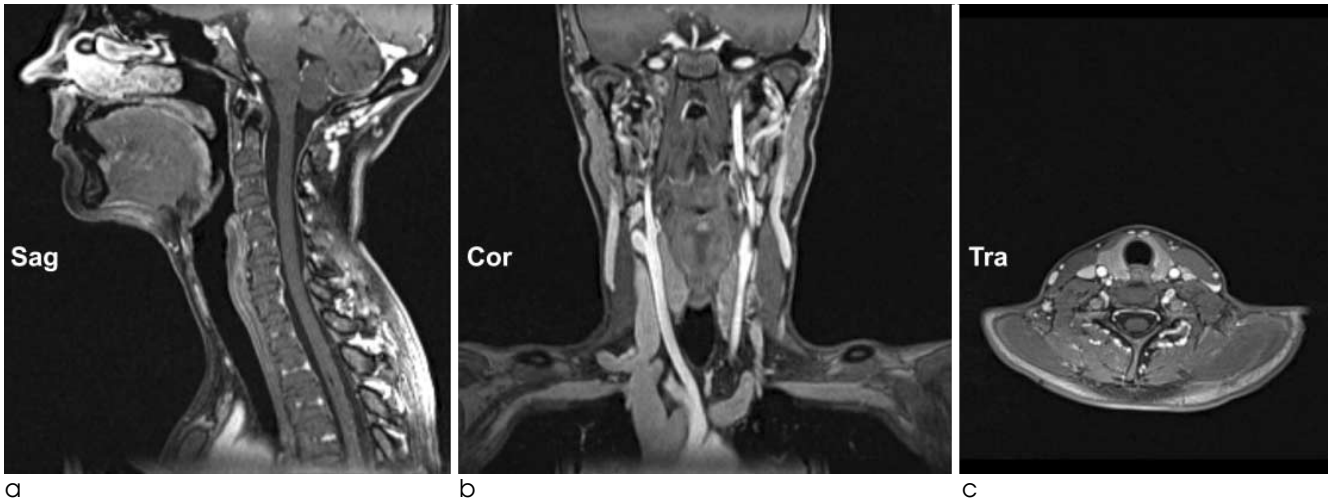

Fig. 14. Multi-planar reconstructions of a radial neck scan with 1.0 mm isotropic resolution, which are unaffected from swallowing or respiration artifacts and which can be used as replacement for separate 2D TSE acquisitions in these orientations. Of note is a failure of spectral fat saturation in the back of the neck, which is a common observation in the proximity of skin folds. Furthermore, the outer slices show slight aliasing along kz, caused by imperfections of the slab-selective excitation pulse. Both effects are not related to the radial scheme.

clinical practice.

Example 6: Imaging of Orbits and Inner Auditory Canal (IAC)

When imaging the orbits with conventional sequences to visualize pathologies of the optic nerves, movements of the eyes and eyelids must be suppressed to avoid degradation of the diagnostic value. Because patient compliance is limited in practice and residual eye motion is often present, improved robustness of these exams can be achieved with use of the radial sequence. Here, we are using isotropic protocols with high spatial resolution of 0.7 – 0.8 mm, which provide very sharp depiction of the optic nerves. In particular, when running the protocols with an echo time that is close to an opposed phase condition, excellent suppression of the intra- and extraconal fat is obtained at 1.5 as well as 3 Tesla. Figure 15c shows one example from 1.5 Tesla with 0.8 mm nominal isotropic resolution, using 800 spokes acquired at 280 Hz/pixel in 4:30 min. Similar protocols are also well suited to image the inner auditory canal (IAC) or full brain, where the use of the radial 3D sequence leads to significant reduction of flow artifacts and to higher detectability of small lesions that potentially could be missed with conventional 2D sequences if they are located in the slice gap.

Example 7: Fat-Suppressed Spine Imaging

Due to the absence of ghosting artifacts, the radial sequence can be also advantageous for high-resolution imaging of the spine. These scans are often done in sagittal orientation so that Cartesian sequences are inherently sensitive to ghosting artifacts from organ movements that can propagate into the area of interest. This is avoided with radial sampling, which

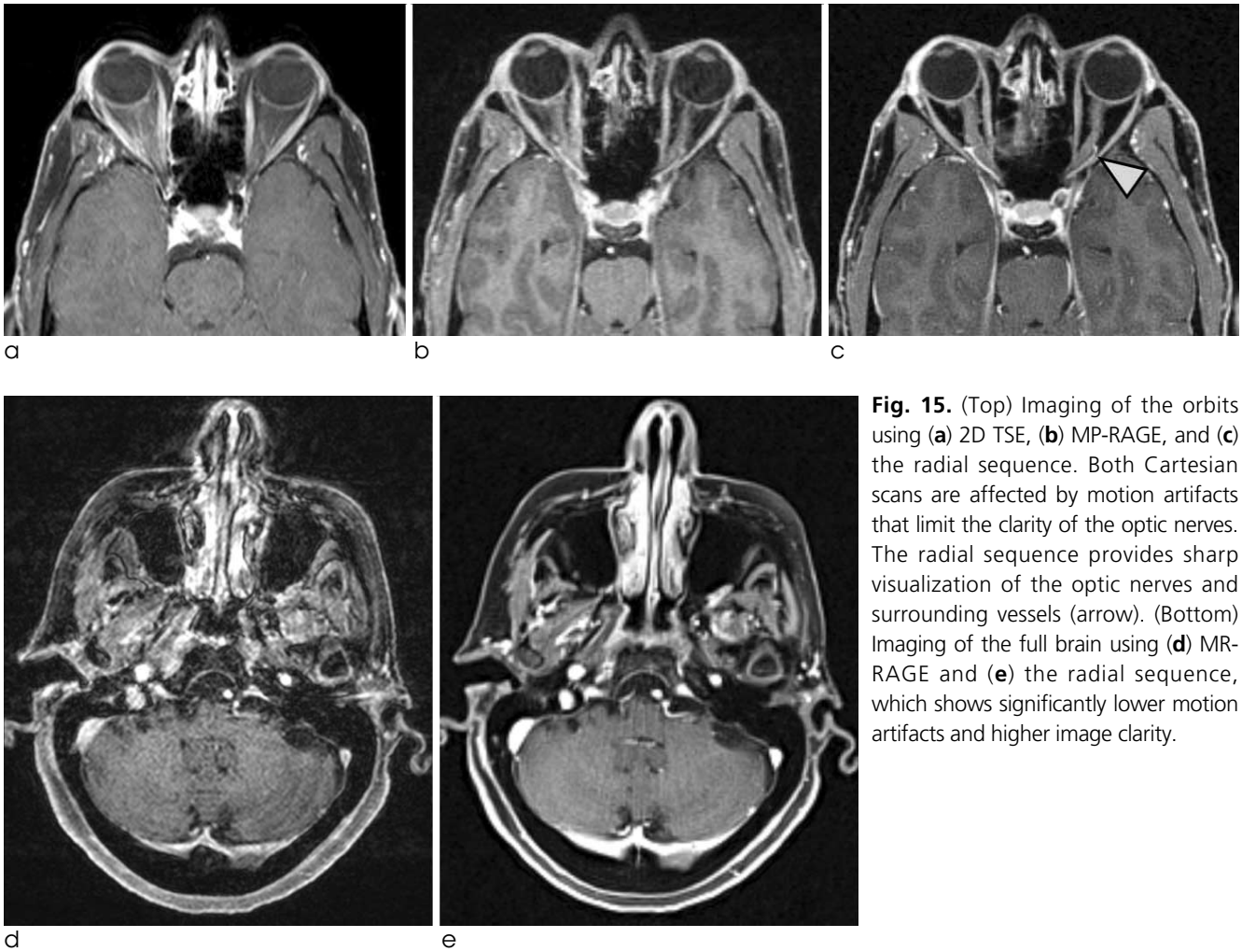

Fig. 15. (Top) Imaging of the orbits using (**a**) 2D TSE, (**b**) MP-RAGE, and (**c**) the radial sequence. Both Cartesian scans are affected by motion artifacts that limit the clarity of the optic nerves. The radial sequence provides sharp visualization of the optic nerves and surrounding vessels (arrow). (Bottom) Imaging of the full brain using (**d**) MR-RAGE and (**e**) the radial sequence, which shows significantly lower motion artifacts and higher image clarity.

http://dx.doi.org/10.13104/jksmrm.2014.18.2.87

Fig. 16. Spine imaging in patients with metastasis using (**a, c**) conventional 2D TSE sequences without fat suppression and (**b, d**) the radial sequence. The radial sequence shows clear contrast enhancement of the metastasis (arrows), while the enhancement is more difficult to see on the TSE scans because of low contrast difference to normal bone marrow and because of ghosting artifacts arising from blood flow and organ movement.

provides cleaner and sharper images. Because the radial sequence uses fat suppression, which is often not used with conventional TSE sequences due to time constraints, the scans are highly sensitive for detection of metastasis and other enhancing lesions, and can be of particular interest for oncologic screening procedures. Figure 16 shows exemplary images from 3 Tesla with a base resolution of 256 pixels, 936 spokes, and a bandwidth of 480 Hz/pixel, acquired in 3:30 min for 40 slices with 1.4 mm thickness.

DISCUSSION

As demonstrated in the large number of patient exams performed over the last two years, the described radial stack-of-stars sequence works reliable in daily clinical use and delivers image contrast comparable to that of conventional T1-weighted 3D GRE sequences, which allows using it as replacement for established protocols with fat-saturated T1 contrast. Due to the higher motion robustness and the more favorable artifact behavior as compared with Cartesian scans, significantly improved image quality is obtained for applications with frequent patient motion, which translates into lower failure rates, higher diagnostic confidence, and ultimately into shorter reading time.

Limitations may arise from the longer acquisition time compared to Cartesian 3D GRE acquisitions, in particular for applications where parallel-imaging techniques can be applied. Although preliminary parallel-imaging methods have been proposed also for radial sequences (27, 28), these methods have not been established yet and still lack the level of robustness achieved with Cartesian approaches. However, shortening the scan duration is less critical for radial acquisitions than for Cartesian sequences where longer acquisition time inherently leads to higher probability of motion artifacts, especially for exams performed during breath holding.

Further limitations may arise from the requirement of fat suppression to prevent off-resonance blurring. In clinical applications where assessment of lesion fat content is needed, T1-weighted scans without fat suppression are conventionally acquired prior to the contrast injection. This is currently not feasible with the radial sequence, but may become possible with the development of a suitable DIXON-based fat/water separation approach. Initial tests with a modified version of the sequence have shown that multiple gradient echoes can be acquired robustly, but a

matching approach to separate fat and water components while deblurring the fat signal remains to be developed. Fat/water separation will additionally help to overcome image-quality problems resulting from insufficient spectrally-selective fat suppression, e.g. in the proximity of skin folds.

The low performance of spectral fat suppression in areas with B_0 inhomogeneities can also result in local high-intensity signal spots, which when convolved with the PSF lead to streak artifacts that contaminate the region of interest. This effect occurs, for instance, when abdominal scans are performed with arms placed next to the body where the fat suppression fails rather often due to the large distance from the isocenter. In most cases, the resulting streaks are minor and don't affect the image quality significantly, although individual slices can also be affected by stronger artifacts. Even in these cases, the images usually remain of diagnostic value. It should be noted that related artifacts also occur for Cartesian techniques and appear as focal striping patterns (29).

Advanced Applications

Dynamic Imaging

A certain disadvantage of radial sampling is that the higher nominal sampling requirement makes it impossible to perform abdominal exams within typical breath-hold durations. Exams can be performed during free breathing instead, but the scans still take too long to separate arterial and venous phases of enhancement, as sometimes needed for lesion characterization. Therefore, the applicability for dynamic contrast-enhanced imaging is limited. However, because the spokes sample the k-space center continuously, advanced reconstruction methods can be applied to overcome this limitation by extracting different dynamic phases from a single continuous scan. For this application, the golden-angle ordering mode is preferable because reconstruction windows can be selected retrospectively (16).

The k-space weighted image contrast (KWIC) method uses a matched view-sharing mechanism to generate time-resolved images from continuously

Table 1. Summary of the Main Imaging Properties of Radial k-space Sampling Compared to Conventional Cartesian Acquisition

Advantages	Disadvantages
+ Much higher robustness to motion	- Slightly longer scan duration
+ Benign artifact behavior (streaks)	- More complex image reconstruction
+ No wrap-around for small FOVs	- No time-to-center value
+ Higher flexibility in protocol setup	- Gradient-delay correction needed
+ Reconstruction of subframes possible	- Requires fat suppression
+ Respiratory self-gating possible	- Sensitive to improper coil selection

Table 2. Suggested Sequence Parameters for Different Clinical Applications

Application	FOV [mm]	Base Resolution [pixels]	Radial Spokes	BW at 1.5T/3T [Hz/px]	Slices	Slice Thickness [mm]	Reduced Slice Resolution	Partial Fourier Slice	Scan Duration [mm:ss]
FB Liver / Abdomen	400	256	400	400/600	80	3.0	60%	6/8	~ 1:00
High-Res. Liver	400	384	900	420/420	96	1.5	65%	off	~ 4:30
Pediatric Body	260	256	800	400/600	96	2.0	63%	6/8	~ 3:25
Pediatric Brain	220	256	800	280/350	160	0.9	66%	6/8	~ 7:00
Neck / Chest	256	256	700	400/610	240	1.0	80%	6/8	~ 7:00
Orbits / IAC	240	288	800	280/400	96	0.8	66%	6/8	~ 4:30
Spine (sag)	350	256	936	230/480	40	1.4	100%	off	~ 3:30

Other parameters: Flip angle = 9 – 12°, Fat suppression = Q-fat sat, TR / TE = min, Positioning mode = ISO
Shim mode = Standard, RF pulse type & Gradient mode = Fast, Excitation = Slab-sel.

http://dx.doi.org/10.13104/jksmrm.2014.18.2.87

acquired data (30). It is fast and can be implemented directly on the MR system, but temporal blurring effects may affect the image quality (31). A more sophisticated approach is the GRASP method (32), which combines parallel imaging and the compressed-sensing principle. High temporal resolution is achieved by assuming that contrast changes occur piecewise-smoothly in time. Initial results look promising (33), but the achievable lesion detectability still needs to be validated more extensively for clinical use. The GRASP method is computationally expensive and currently requires reconstruction on external computers.

Self-Gating for Respiration Compensation

The continuous acquisition of the k-space center can also be exploited to obtain information about the respiratory phases if the patient breathes during an abdominal or chest scan. Because the total signal power of the excited volume changes if the lung volume increases and decreases, a respiration curve can be generated from center samples of the acquired spokes. An exemplary algorithm has been described in (34). The respiration signal can be used, e.g., to quantify the breathing activity during the scan, or to sort the data into different bins and to create respiration-gated reconstructions without motion blurring (35). Unlike conventional navigators, which are interleaved with the scan, the self-gating approach does not prolong the scan time or disturb the steady state of the magnetization.

CONCLUSIONS

Radial k-space sampling is a concept that has been known since the early days of MRI but has not been used routinely for clinical applications so far. Based on the experience gained during this work, we propose that with the current generation of MR systems 3D radial stack-of-stars GRE imaging is robust enough for daily clinical use when following the described implementation and configuration guidelines. It offers similar image contrast to conventional fat-suppressed T1-weighted sequences but significantly reduced sensitivity to motion and more benign artifact behavior. While it might not replace conventional sequences in patients who are able to suspend movements and comply with instructions, it can be a sequence of choice in uncooperative patients and for applications where organ motion is unavoidable. Development of a reliable fat/water separation as well as tailored parallel-imaging approaches will further increase its utility for clinical practice.

References

1. Kumar A, Welti D, Ernst RR. NMR Fourier zeugmatography. J Magn Reson 1975;18:69-83
2. Meyer CH, Hu BS, Nishimura DG, Macovski A. Fast spiral coronary artery imaging. Magn Reson Med 1992;28:202-213
3. Crémillieux Y, Briguet A, Deguin A. Projection-reconstruction methods: fast imaging sequences and data processing. Magn Reson Med 1994;32:23-32
4. Mistretta CA, Wieben O, Velikina J, et al. Highly constrained backprojection for time-resolved MRI. Magn Reson Med 2006;55:30-40
5. Du J, Carroll TJ, Brodsky E, et al. Contrast-enhanced peripheral magnetic resonance angiography using time-resolved vastly undersampled isotropic projection reconstruction. J Magn Reson Imaging 2004;20:894-900
6. Lustig M, Donoho D, Pauly JM. Sparse MRI: the application of compressed sensing for rapid MR imaging. Magn Res Med 2007;58:1182-1195
7. Pipe JG. Motion correction with PROPELLER MRI: application to head motion and free-breathing cardiac imaging. Magn Reson Med 1999;42:963-969
8. Nishimura DG, Jackson JI, Pauly JM. On the nature and reduction of the displacement artifact in flow images. Magn Reson Med 1991;22:481-492
9. Chandarana H, Block KT, Rosenkrantz AB, et al. Free-breathing radial 3D fat-suppressed T1-weighted gradient echo sequence: a viable alternative for contrast-enhanced liver imaging in patients unable to suspend respiration. Invest Radiol 2011;46:648-653
10. Azevedo RM, de Campos RO, Ramalho M, Herédia V, Dale BM, Semelka RC. Free-breathing 3D T1-weighted gradient-echo sequence with radial data sampling in abdominal MRI: preliminary observations. AJR Am J Roentgenol 2011;197:650-657
11. Chandarana H, Block KT, Winfeld MJ, et al. Free-breathing contrast-enhanced T1-weighted gradient-echo imaging with radial k-space sampling for paediatric abdominopelvic MRI. Eur Radiol 2014;24:320-326
12. Wu X, Raz E, Block KT, et al. Contrast-enhanced radial 3D fat-suppressed T1-weighted gradient-echo (Radial-VIBE) sequence: a viable and potentially superior alternative to conventional fat-suppressed contrast-enhanced T1-weighted studies of the head and neck. Am J Roentgenol 2014:in press
13. Chandarana H, Heacock L, Rakheja R, et al. Pulmonary nodules in patients with primary malignancy: comparison of hybrid PET/MR and PET/CT imaging. Radiology 2013;268:874-881
14. Bamrungchart S, Tantaway EM, Midia EC, et al. Free breathing three-dimensional gradient echo-sequence with radial data sampling (radial 3D-GRE) examination of the pancreas:

Comparison with standard 3D-GRE volumetric interpolated breathhold examination (VIBE). J Magn Reson Imaging 2013;38:1572-1577
15. Bernstein MA, King KF, Xiaohong JZ. Handbook of MRI pulse sequences. Elsevier Academic Press, Waltham, 2004
16. Winkelmann S, Schaeffter T, Koehler T, Eggers H, Doessel O. An optimal radial profile order based on the Golden Ratio for time-resolved MRI. IEEE T Med Imaging 2007;26:68-76
17. Block KT. Advanced methods for radial data sampling in magnetic resonance imaging. SUB University of Goettingen. http://webdoc.sub.gwdg.de/diss/2008/block/block.pdf. Published September 16, 2008. Accessed January 9, 2014
18. Ramachandran GN, Lakshminarayanan AV. Three-dimensional reconstruction from radiographs and electron micrographs: application of convolutions instead of Fourier transforms. Proc Natl Acad Sci USA 1971;68:2236-2240
19. Beatty PJ, Nishimura DG, Pauly JM. Rapid gridding reconstruction with a minimal oversampling ratio. IEEE T Med Imaging 2005;24:799-808
20. Jackson JI, Meyer CH, Nishimura DG, Macovski A. Selection of a convolution function for Fourier inversion using gridding. IEEE T Med Imaging 1991;10:473-478
21. Peters DC, Korosec FR, Grist TM, et al. Undersampled projection reconstruction applied to MR angiography. Magn Reson Med 2000;43:91-101
22. Alley MT, Glover GH, Pelc NJ. Gradient characterization using a Fourier-transform technique. Magn Reson Med 1998;39:581-587
23. Peters DC, Derbyshire JA, McVeigh ER. Centering the projection reconstruction trajectory. Magn Reson Med 2003;50:1-6
24. Block KT, Uecker M. Simple method for adaptive gradient-delay compensation in radial MRI. In: Proceedings of the 19th scientific meeting, International Society for Magnetic Resonance in Medicine 2011, Montréal, p 2816
25. Brodsky EK, Holmes JH, Yu H, Reeder SB. Generalized k-space decomposition with chemical shift correction for non-Cartesian water-fat imaging. Magn Reson Med 2008;59:1151-1164
26. Xue Y, Yu J, Kang HS, Englander S, Rosen MA, Song HK. Automatic coil selection for streak artifact reduction in radial MRI. Magn Reson Med 2012;67:470-476
27. Pruessmann KP, Weiger M, Börnert P, Boesiger P. Advances in sensitivity encoding with arbitrary k-space trajectories. Magn Reson Med 2001;46:638-651
28. Seiberlich N, Breuer FA, Ehses P, et al. Using the GRAPPA operator and the generalized sampling theorem to reconstruct undersampled non-Cartesian data. Magn Reson Med 2009;61:705-715
29. Harvey JA, Hendrick RE, Coll JM, Nicholson BT, Burkholder BT, Cohen MA. Breast MR imaging artifacts: how to recognize and fix them. Radiographics 2007;27:S131-145
30. Song HK, Dougherty L. Dynamic MRI with projection reconstruction and KWIC processing for simultaneous high spatial and temporal resolution. Magn Reson Med 2004;52:815-824
31. Altbach MI, Bilgin A, Li Z, Clarkson EW, Trouard TP, Gmitro AF. Processing of radial fast spin-echo data for obtaining T2 estimates from a single k-space data set. Magn Reson Med 2005;54:549-559
32. Feng L, Grimm R, Block KT, et al. Golden-angle radial sparse parallel MRI: combination of compressed sensing, parallel imaging, and golden-angle radial sampling for fast and flexible dynamic volumetric MRI. Magn Reson Med 2013:Epub ahead of print, DOI: 10.1002/mrm.24980
33. Chandarana H, Feng L, Block KT, et al. Free-breathing contrast-enhanced multiphase MRI of the liver using a combination of compressed sensing, parallel imaging and golden-angle radial sampling. Invest Radiol 2013;48:10-16
34. Grimm R, Block KT, Hutter J, et al. Self-gating reconstructions of motion and perfusion for free-breathing T1-weighted DCE-MRI of the thorax using 3D stack-of-stars GRE imaging. In: Proceedings of the 20th scientific meeting, International Society for Magnetic Resonance in Medicine 2012, Melbourne, p 3814
35. Lin W, Guo J, Rosen MA, Song HK. Respiratory motion-compensated radial dynamic contrast-enhanced (DCE)-MRI of chest and abdominal lesions. Magn Reson Med 2008;60:1135-1146

http://dx.doi.org/10.13104/jksmrm.2014.18.2.87